



Photoacoustic tomography with a model-based approach involving realistic detector properties

Pankaj Warbal, Ratan K. Saha*

Department of Applied Sciences, Indian Institute of Information Technology Allahabad, Prayagraj, 211015, India

ARTICLE INFO

MSC:
00-01
99-00

Keywords:

Regularization
Deblurring
Directivity
Finite sensor
Photoacoustic tomography

ABSTRACT

A computational and experimental study is conducted to examine how directivity associated with a finite aperture sensor affects photoacoustic tomography (PAT) image reconstruction. Acoustic signals for the simulation work were computed using a discrete particle approach from three numerical phantoms including a vasculature. The theoretical framework and a Monte Carlo approach for construction of a tissue configuration are discussed in detail. While simulating forward data, the directivity of the sensor was taken into account. The image reconstruction was accomplished using system matrix based methods like l_2 norm Tikhonov regularization, l_1 norm regularization and total variation (TV) minimization. Accordingly, two different system matrices were constructed- (i) assuming transducer as a point detector (PD) and (ii) retaining properties of a finite detector with directivity (FDWD). Image reconstruction was also performed utilizing experimentally measured PA signals. Both the computational and experimental results demonstrate that blur-free PAT imaging can be achieved with the FDWD method. Additionally, TV minimization provides marginally better image reconstruction compared to the other schemes.

1. Introduction

Photoacoustic tomography (PAT), also called optoacoustic tomography, is a non-invasive imaging modality. It is a hybrid technique combining the high contrast of optical imaging and high resolution of ultrasound imaging (Wang, 2017). The underlying phenomenon of PAT imaging is the photoacoustic (PA) effect. In the PA effect, a biological sample containing chromophores is illuminated with short laser pulses that induce rapid thermo-elastic expansion of the tissue generating acoustic/pressure waves. The wide-band PA signals are collected by ultrasound transducers that surround the tissue in a typical PAT setup. The captured signals are then used to produce/reconstruct the map of the initial pressure rise. The PAT modality has many biomedical imaging applications (Yao and Wang, 2021; Manohar and Dantuma, 2019; Yao and Wang, 2018; Nyayapathi et al., 2019; Sangha et al., 2022; Li et al., 2021; Na et al., 2022; Bohndiek et al., 2015; Nandy et al., 2018). Recently, exquisite images of small-animal whole-body have been generated at high spatiotemporal resolution using a 512-element full-ring ultrasonic transducer array, central frequency = 5 MHz, one-way bandwidth > 90% (Li et al., 2017). Similar setup has also been employed for PAT imaging of human breasts (Lin et al., 2018).

The PAT image reconstruction methods can be divided into two categories — analytical techniques and model based schemes. The backprojection (BP) (Xu and Wang, 2005; Warbal et al., 2019) and time reversal (TR) (Treeby and Cox, 2010) algorithms fall under the first category and are commonly used for PAT image reconstruction. These methods are non-iterative, fast and easy to implement but lack to provide quantitatively accurate images. The l_2 norm based Tikhonov regularization, l_1 norm based regularization and total variation (TV) minimization procedures are the examples of the second category (Paltauf et al., 2002; Rosenthal et al., 2010; Prakash et al., 2018). These methods are iterative and require the generation and inversion of a system matrix (which is a large ill-conditioned matrix). Hence, the protocols become computationally expensive. They can facilitate quantitatively accurate images even for a limited-view data set.

In general, a single-element, unfocused transducer of finite aperture circularly scans the imaging region and records pressure signals. The angular response of a detector with a finite aperture is not uniform (rather direction-dependent) (Szabo, 2004). It is most sensitive along its axis and gradually becomes less sensitive as the angle of the source point (in the far field) increases. In addition to that, a realistic transducer transforms a delta pulse into a pulse of finite width due to its finite aperture. Therefore, the width and magnitude of the broad pulse

* Corresponding author.

E-mail address: ratank.saha@iiita.ac.in (R.K. Saha).

URL: <https://profile.iiita.ac.in/ratank.saha/> (R.K. Saha).

(i.e., the output pulse of the transducer) depend upon the direction from which the input pulse is coming. As a result of that, a practical detector, if it is approximated as a point detector during reconstruction, introduces banding artifacts and significant blurring in a PAT image (Treeby and Cox, 2010; Cox and Treeby, 2010; Warbal and Saha, 2022a). Treeby et al. observed banding artifacts in PAT images arising due to the directionality of the transducer elements even after having the full-view of the measurement surface (Treeby and Cox, 2009; Cox and Treeby, 2010). Schoonover et al. also noticed the same unwanted banding artifacts in the reconstructed images (Schoonover et al., 2012). It is worthy to mention here that there are other sources of blurring as well in the PAT imaging- (i) finite temporal width of the input laser beam, (ii) limited bandwidth of the detector and (iii) acoustically lossy and dispersive medium (Warbal and Saha, 2022b).

Several works have been performed to examine the effect of finite size transducer on PAT imaging. Accordingly, proposed various strategies to mitigate this issue. For example, i) a small transducer can be used, (ii) a large scanning radius can be set; however, these solutions will reduce the signal-to-noise ratio and therefore, are undesirable (Yang et al., 2007). A negative acoustic lens mounted on a planner transducer was also utilized to address this problem (Pramanik et al., 2009). Wang et al. and Roitner et al. applied deconvolution approaches to overcome the negative effect of finite aperture transducer in PAT images (Wang et al., 2004b; Roitner et al., 2014). A spatiotemporal optimal filter was also designed to deal with this problem (Li et al., 2010). Lua et al. introduced a space-variant filter-based modified back-projection method to improve image quality and reduce time consumption in optoacoustic mesoscopy by effectively addressing the spatial impulse response (Lu et al., 2020). This has been studied previously as well (Araque Caballero, 2013). Seeger et al. expanded the capabilities of optical-resolution optoacoustic microscopy, by reporting spatially-dependent total impulse response (TIR) correction, with a novel method using spatially-distributed optoacoustic point sources (SOAPs) in 2020 (Seeger et al., 2020). Chowdhury et al. introduced a novel synthetic total impulse response characterization method for improving the accuracy of hand-held optoacoustic images (Chowdhury et al., 2020). Wang et al. carried out a detailed study on this topic (Wang et al., 2010). This group built a system matrix by incorporating the properties of the ultrasonic transducer and subsequently, formed PAT images via model matrix inversion procedure. This strategy was found to be effective in improving the spatial resolution of the images. The model matrix based approach was also employed by us to study the same (Warbal and Saha, 2022a).

The problem of degradation of image quality in PAT imaging due to the usage of a transducer of finite aperture is revisited here. This has been investigated by employing computational and experimental means. The study considers 2D imaging regions. The advantages of this approach (2D setup) are- (i) low cost because a single-element transducer typically circularly scans the region of interest and captures the PA signals, (ii) single channel data acquisition card is needed, (iii) computational load is manageable and thus model-based methods can be utilized and (iv) effectiveness of a new algorithm can easily be validated experimentally. For these reasons, 2D setup has been extensively used for proof-of-concept experiments (Warbal et al., 2019; Pramanik, 2014; Xia and Wang, 2012). As mentioned earlier, the directivity effect for a single-element transducer induces unwanted distortions in the reconstructed images. The present study serves as a proof-of-concept work, focusing on how to remove such distortions utilizing model-based methods.

This work first discusses a generalized version of the theoretical model for PA signal simulation presented in Warbal and Saha (2022a). Essentially, the PA signal from a source with a regular shape is calculated using the exact method and subsequently, convolved with the spatial impulse response function (SIRF) of a realistic transducer. Such signals emitted by a collection of absorbers are added linearly to form a resultant signal. This is called the discrete particle approach

which properly models the effect of the transducer with finite aperture while generating forward data. This theoretical framework has been extensively used in ultrasonic tissue characterization (Wagner et al., 1987; Shung and Thieme, 1992). The PA signals from three test phantoms, namely, three-point, multi-disc and vasculature, were generated for image reconstruction. A realization of the vasculature phantom was simulated by deploying a Monte Carlo method known as the random sequential adsorption (RSA) technique. Thus, the structural details became available in the microscopic regime. The system matrix based methods like l_2 norm based Tikhonov regularization, l_1 norm based regularization and TV methods were realized herein for image reconstruction. In building the system matrix, the angular response of the sensor was incorporated. It is referred to as the finite detector with directivity (FDWD) method in the remaining text. The system matrix was also been constructed for point detector and accordingly, images were created for comparison (this is mentioned as a PD technique in the rest of the manuscript). The experiments were conducted too to validate our findings. The numerical and experimental results confirm that the impact of finite size detector can best be mitigated if FDWD and TV minimization work together.

2. Mathematical ingredients

2.1. Forward problem

2.1.1. Calculation of PA field for a spherical absorber

Assuming thermal and stress confinements, the PA field at a point \mathbf{r} due to a spherical absorber of radius a and located at \mathbf{r}_0 is given by Wang (2017),

$$\mathcal{P}(\mathbf{r}) = EI_0 \mathcal{Q}(\omega) \frac{e^{ik_f |\mathbf{r}-\mathbf{r}_0|}}{|\mathbf{r}-\mathbf{r}_0|}, \quad (1)$$

where $E = \frac{i\mu_a \beta v_s a^2}{C_p}$; μ_a , β , C_p and v_s indicate the optical absorption coefficient, isobaric thermal expansion coefficient, specific heat and speed of sound for the fluid medium inside the PA source, respectively; k_f is the wave number for the acoustic wave in the surrounding fluid medium. The notation I_0 stands for the intensity of the incident optical radiation, ω is its modulation frequency and $\mathcal{Q}(\omega)$ is defined as,

$$\mathcal{Q}(\omega) = \frac{[\sin(\hat{q}) - \hat{q} \cos(\hat{q})] e^{-ik_f a}}{\hat{q}^2 [(1 - \hat{\rho}) \sin(\hat{q})/\hat{q} - \cos(\hat{q}) + i\hat{\rho}\hat{v} \sin(\hat{q})]}$$

with $\hat{q} = k_s a$, $\hat{\rho} = \rho_s/\rho_f$ and $\hat{v} = v_s/v_f$. Here, v , ρ and k represent the speed of sound, density and wave number, respectively. The subscripts s and f refer to the source and the ambient medium, respectively.

2.1.2. Computing PA signal for a finite detector

Monodisperse absorbers. If an ensemble of monodisperse absorbers with identical physical properties is uniformly illuminated by a laser beam then the collective PA field can be computed by applying the linear superposition principle as (Warbal and Saha, 2022a),

$$\mathcal{P}(\mathbf{r}) = \sum_{n=1}^N EI_0 \mathcal{Q}(\omega) \frac{e^{ik_f |\mathbf{r}-\mathbf{r}_n|}}{|\mathbf{r}-\mathbf{r}_n|}, \quad (2)$$

where N is the total number of spherical sources. The PA signal corresponding to a delta function heating pulse becomes,

$$\mathcal{P}(\mathbf{r}, t) = \sum_{n=1}^N \frac{EF}{2\pi} \int_{-\infty}^{\infty} \mathcal{Q}(\omega) \frac{e^{ik_f |\mathbf{r}-\mathbf{r}_n|}}{|\mathbf{r}-\mathbf{r}_n|} e^{-i\omega t} d\omega, \quad (3)$$

where F is fluence of the exciting light pulse. This methodology is called the discrete particle approach because the resultant PA signal is calculated by summing the signals emitted by the individual sources.

Eq. (3) is valid when the pressure field is measured by a point detector. However, a real detector has a finite aperture. The expression for the PA signal captured by such a finite sensor can be cast as (Warbal and Saha, 2022a),

$$\mathcal{P}(t) = \int \int_{SA} \mathcal{P}(\mathbf{r}, t) d^2\mathbf{r}, \quad (4)$$

where, SA is the surface area of the aperture of the sensor. Using Eqs. (3) and (4), we get,

$$\begin{aligned} \mathcal{P}_{nbl}(t) &= \int \int_{SA} d^2\mathbf{r} \sum_{n=1}^N \frac{EF}{2\pi} \int_{-\infty}^{\infty} \mathcal{Q}(\omega) \frac{e^{ik_f|\mathbf{r}-\mathbf{r}_n|}}{|\mathbf{r}-\mathbf{r}_n|} e^{-i\omega t} d\omega \\ &= EF \sum_{n=1}^N \int_{-\infty}^{\infty} d\omega e^{-i\omega t} \mathcal{Q}(\omega) \int \int_{SA} \frac{e^{ik_f|\mathbf{r}-\mathbf{r}_n|}}{2\pi|\mathbf{r}-\mathbf{r}_n|} d^2\mathbf{r} \\ &= EF \sum_{n=1}^N \int_{-\infty}^{\infty} d\omega e^{-i\omega t} \mathcal{Q}(\omega) G_D(\omega), \end{aligned} \quad (5)$$

where $G_D(\omega) = \int \int_{SA} \frac{e^{ik_f|\mathbf{r}-\mathbf{r}_n|}}{2\pi|\mathbf{r}-\mathbf{r}_n|} d^2\mathbf{r}$ is the directivity function for the finite sensor (Karmakar et al., 2015). The subscript nbl demonstrates that the signal is non-bandlimited in nature. Eq. (5) can further be written in a compact form as,

$$\mathcal{P}_{nbl}(t) = \sum_{n=1}^N [p(t) * g(\mathbf{r}_n, t)], \quad (6)$$

where

$$p(t) = \frac{EF}{2\pi} \int_{-\infty}^{\infty} \mathcal{Q}(\omega) e^{-i\omega t} d\omega, \quad (7)$$

and

$$g(\mathbf{r}_n, t) = \int \int_{SA} \frac{\delta(t - |\mathbf{r} - \mathbf{r}_n|/v_f)}{2\pi|\mathbf{r} - \mathbf{r}_n|} d^2\mathbf{r}, \quad (8)$$

with $*$ is the convolution operation and $g(\mathbf{r}_n, t)$ is the SIRF of the detector.

Polydisperse absorbers. The above theoretical framework can readily be generalized in order to calculate the resultant PA signal generated by a collection of polydisperse PA sources when excited homogeneously by the input radiation. In that case, Eq. (6) converts into,

$$\mathcal{P}_{nbl}(t) = \sum_{n=1}^N [p_n(t) * g(\mathbf{r}_n, t)]. \quad (9)$$

Here, $p_n(t)$ takes the form,

$$p_n(t) = \frac{E_n F}{2\pi} \int_{-\infty}^{\infty} \mathcal{Q}_n(\omega) e^{-i\omega t} d\omega, \quad (10)$$

with $E_n = \frac{i\mu_a \beta v_s a_n^2}{C_p}$ and

$$\mathcal{Q}_n(\omega) = \frac{[\sin(\hat{q}_n) - \hat{q}_n \cos(\hat{q}_n)] e^{-ik_f a_n}}{\hat{q}_n^2 [(1 - \hat{\rho}) \sin(\hat{q}_n) / \hat{q}_n - \cos(\hat{q}_n) + i\hat{\rho}\hat{v} \sin(\hat{q}_n)]}.$$

Note that in the above derivation, it has been assumed that the sources are of different sizes but the opto-thermo-mechanical parameters are the same.

2.1.3. Estimation of band-limited signal

Note that the expression for $\mathcal{P}_{nbl}(t)$ contains all possible frequencies. However, a real transducer is a bandlimited detector. The bandlimited signal can easily be yielded by filtering the nbl signal with a cosine Gabor filter as given below,

$$\mathcal{P}(t) = \text{Re} [\mathcal{P}_{nbl}(t)] * \frac{\sigma_{bw}}{\sqrt{2\pi}} \exp\left(-\frac{\sigma_{bw}^2 t^2}{2}\right) \cos(2\pi f_0 t), \quad (11)$$

where the real part of the nbl signal is taken; f_0 is the center frequency of the transducer and σ_{bw} is related to its -6 dB bandwidth (denoted by bw). In this work, Eq. (11) has been evaluated numerically to compute the bandlimited resultant PA signal generated by many uniformly illuminated monodisperse/polydisperse spherical absorbers.

2.2. Inverse problem

The problem of PAT image reconstruction can be modeled as a system of linear equations (Prakash et al., 2014),

$$\mathcal{A}\mathcal{X} = \mathcal{P}, \quad \mathcal{A} \in \mathbb{R}^{m \times n}, \quad \mathcal{P} \in \mathbb{R}^m \quad \text{and} \quad \mathcal{X} \in \mathbb{R}^n \quad (12)$$

where \mathcal{A} is the system matrix; \mathcal{X} is the initial pressure map of the illuminated region in the form of a long column vector and \mathcal{P} contains measured pressure data (also a long column vector). The system matrix in general incorporates various properties of the incident laser beam, medium and detectors. The exact solution is possible for Eq. (12) when \mathcal{A} is a square matrix (i.e., $m = n$) and invertible ($|\mathcal{A}| \neq 0$). In case of failing to meet this condition (e.g., $m > n$), the method of least squares can be employed to get the following solution,

$$\mathcal{X}_{sol} = \arg \min(\|\mathcal{A}\mathcal{X} - \mathcal{P}\|_2^2), \quad (13)$$

where $\|\cdot\|_2$ is the l_2 norm. However, the traditional methods for solving Eq. (13) may not give meaningful solutions for discrete ill-posed problems (Hansen, 2007). Three different methods for solving Eq. (12) have been invoked herein and these algorithms are described below in brief.

2.2.1. l_2 norm based solution

The Tikhonov regularization method has been almost exclusively utilized to solve Eq. (12) when $m \neq n$. The corresponding solution can be written as (Rosenthal et al., 2010),

$$\mathcal{X}_{sol} = \arg \min(\|\mathcal{A}\mathcal{X} - \mathcal{P}\|_2^2 + \lambda^2 \|\mathcal{X}\|_2^2). \quad (14)$$

Here, λ is the regularization parameter. The first term on the right hand side of Eq. (14) is called the fidelity term and the second one is the penalty term. The impact of the penalty term depends upon the magnitude of λ . A higher λ value renders over smoothing of the image whereas a lower λ value amplifies the noise. A suitable value of λ can be estimated by employing the L-curve or GCV technique. The L-curve method is a graphical approach. In this procedure, a plot of solution norm versus residual norm is generated in a log-log scale. The location of maximum curvature of that graph provides the optimum λ . This method may be time taking and is sensitive to curvature estimation. The GCV method is a data-driven approach that uses the principle of minimizing the error between the reconstructed image and the ground truth. The numerical value of the regularization parameter is obtained by minimizing the GCV score. It may pose difficulty in finding the optimum λ when the GCV function becomes flat (Ramani et al., 2012; Hansen and O'Leary, 1993).

For this method, a closed form solution can be derived as,

$$\mathcal{X}_{sol} = (\mathcal{A}^T \mathcal{A} + \lambda^2 \mathcal{I})^{-1} \mathcal{A}^T \mathcal{P}, \quad (15)$$

where \mathcal{A}^T is the transpose of \mathcal{A} . Eq. (15) can further be simplified by performing singular value decomposition (SVD) of \mathcal{A} ,

$$\mathcal{A} = \mathcal{J} \mathcal{W} \mathcal{H}^T = \sum_{i=1}^n j_i w_i h_i^T, \quad (16)$$

where $\mathcal{J} = (j_1, j_2, \dots, j_n)$ and $\mathcal{H} = (h_1, h_2, \dots, h_n)$ are the left and right unitary matrices, respectively; $\mathcal{W} = \text{diag}(w_1, w_2, \dots, w_n)$ is the singular matrix with $w_1 \geq w_2 \geq \dots \geq w_n$.

Replacing \mathcal{A} in Eq. (15) with Eq. (16), one obtains,

$$\begin{aligned} \mathcal{X}_{sol} &= (\mathcal{H} \mathcal{W}^T \mathcal{W} \mathcal{H}^T + \lambda^2 \mathcal{I})^{-1} \mathcal{H} \mathcal{W}^T \mathcal{J}^T \mathcal{P} \\ &= \mathcal{H} (\mathcal{W}^T \mathcal{W} + \lambda^2 \mathcal{I})^{-1} \mathcal{W}^T \mathcal{J}^T \mathcal{P} \\ &= \sum_{i=1}^n \frac{w_i (j_i^T \mathcal{P})}{w_i^2 + \lambda^2} h_i. \end{aligned} \quad (17)$$

The filter factors $\frac{w_i}{w_i^2 + \lambda^2}$ in Eq. (17) retain the contributions from the larger singular values and those of small singular values are discarded.

2.2.2. l_1 norm based solution

Another approach for finding out the solution of Eq. (12) is to add a l_1 norm penalty term into Eq. (13) and then minimize the cost function. The solution appears like,

$$\mathcal{X}_{sol} = \arg \min(\|\mathcal{A}\mathcal{X} - \mathcal{P}\|_2^2 + \lambda \|\mathcal{X}\|_1). \quad (18)$$

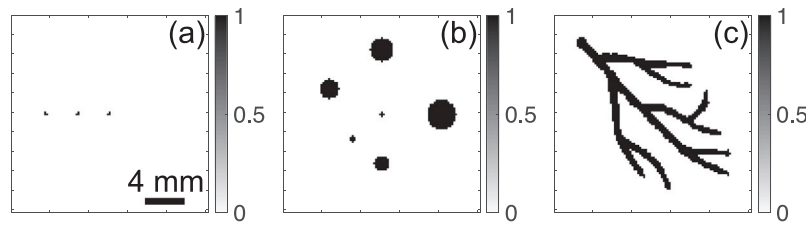


Fig. 1. Numerical phantoms considered in this study- (a) three-point phantom, (b) multi-disc phantom and (c) vasculature phantom. The images are accompanied by a color bar indicating the numerical values of the gray levels.

The cost function is not always differentiable and thus an analytical solution does not exist in this case. One has to rely on numerical solutions. Several numerical strategies have been developed for yielding solutions (Daubechies et al., 2004; Beck and Teboulle, 2009; Goldstein et al., 2014; Afonso et al., 2010). The l_1 norm regularization is known to provide sparse solutions. Many PAT studies utilized this regularization scheme for image reconstruction (Prakash et al., 2018; Guo et al., 2010).

2.2.3. TV minimization based solution

In order to solve Eq. (12), the total variation minimization method can also be used. As in the previous cases, a penalty term, involving a derivative of the unknown, is added to the fidelity term. After that solution is sought by minimizing the cost function. The solution looks like (Li et al., 2013),

$$\mathcal{X}_{sol} = \arg \min \left(\frac{1}{2} \eta \| \mathcal{A} \mathcal{X} - \mathcal{P} \|_2^2 + \sum_i \| D_i \mathcal{X} \|_1 \right). \quad (19)$$

where D_i is the discrete gradient operator on \mathcal{X} at the i th position; the parameter η is positive definite. The penalty term ensures that the solution will exhibit less variation in space. In particular, a positive definite parameter in the regularization term penalizes only high-frequency variations often associated with the noise in the reconstructed image, while leaving low-frequency variations corresponding to important image features unchanged. A positive definite parameter ensures that the regularization term is well-behaved and has a unique minimum, which is important for the convergence and stability of the minimization process (Wood, 2004). Analytical solution cannot be derived in this case as well and thus solutions are obtained by deploying different numerical means. This framework can faithfully suppress noise and streak artifacts in the reconstructed image (Han et al., 2015). The algorithm has been explored by many groups for PAT imaging (Yao and Jiang, 2011; Prakash et al., 2018; Kong et al., 2018). Some of the variants of TV available in the literature are anisotropic TV, isotropic TV, higher-order TV, and total generalized variation (TGV). We used the anisotropic variant in our work. The time taken by different variants depend on several factors, including the size of the image, the complexity of the TV term, the specific algorithm used, and the hardware used for computation (Lv et al., 2013; González et al., 2017).

2.3. Image quality metrics

Deciding that one image is better than the other, differs from one person to another. Hence, we need a quantitative approach to compare the quality of an image. Various image quality metrics have been developed so far for this purpose (Thung and Raveendran, 2009). Some of the standard metrics used to assess the performance of reconstruction methods are root mean square error (RMSE), Pearson correlation coefficient (PCC), contrast to noise ratio (CNR) and structure similarity index measure (SSIM) (Warbal and Saha, 2022a). The image quality metrics were only calculated for the simulated images. These are described below.

Root mean square error (RMSE). The RMSE can be computed as follows,

$$RMSE = \sqrt{\frac{\sum_{i=1}^M [\mathcal{X}(i) - \mathcal{X}_{sol}(i)]^2}{M}}, \quad (20)$$

where \mathcal{X} , \mathcal{X}_{sol} and M are the ground truth, reconstructed images and the number of pixels in an image, respectively. The RMSE approaches to zero when \mathcal{X} and \mathcal{X}_{sol} are identical.

Pearson correlation coefficient (PCC). The PCC provides information about the similarity between the target and the reconstructed images. The formula for PCC is,

$$PCC = \frac{COV(\mathcal{X}, \mathcal{X}_{sol})}{\sigma_{\mathcal{X}} \sigma_{\mathcal{X}_{sol}}}, \quad (21)$$

where COV , $\sigma_{\mathcal{X}}$, and $\sigma_{\mathcal{X}_{sol}}$ are the covariance between \mathcal{X} and \mathcal{X}_{sol} image matrices, standard deviation of \mathcal{X} and standard deviation of \mathcal{X}_{sol} , respectively. The range of the PCC value is from -1 to 1 . The PCC values closer to 1 indicate better reconstructions.

Contrast to noise ratio (CNR). The CNR is defined as (Song et al., 2004),

$$CNR = \frac{\xi_{roi} - \xi_{back}}{(\sigma_{roi}^2 n_{roi} + \sigma_{back}^2 n_{back})^{\frac{1}{2}}}, \quad (22)$$

where ‘roi’ and ‘back’ stand for the source and the background domains of the reconstructed image, respectively. Here, ξ is the mean pressure value; $n_{roi} = A_{roi}/A_{total}$ and $n_{back} = A_{back}/A_{total}$ where A_{roi} and A_{back} are the total number of pixels in the source image with initial pressure not equal to 0 and equal to 0, respectively; A_{total} is the total number of pixels in the original/reconstructed image.

Structure similarity index measure (SSIM). The similarity in structure between the ground truth and the reconstructed image can be quantified using the SSIM parameter. The expression for the SSIM is given by Wang et al. (2004a),

$$SSIM = \frac{(2\xi_{\mathcal{X}} \xi_{\mathcal{X}_{sol}} + c_1)(2 COV(\mathcal{X}, \mathcal{X}_{sol}) + c_2)}{(\xi_{\mathcal{X}}^2 + \xi_{\mathcal{X}_{sol}}^2 + c_1)(\sigma_{\mathcal{X}}^2 + \sigma_{\mathcal{X}_{sol}}^2 + c_2)}. \quad (23)$$

The constants c_1 and c_2 stabilize Eq. (23) in case of weak denominator. The pressure values associated with the pixels in the nominal and the reconstructed images were first brought into the same scale (using shifting and scaling) ranging from 0 to 1 covering 256 gray levels. Later those matrices were given as inputs to the SSIM function of MATLAB to estimate the SSIM between the two images.

3. Computational and experimental methods

3.1. Computational methods

3.1.1. Numerical phantoms

Three binary phantoms were employed in the present work. Fig. 1 displays 2D cross-sections of these imaging regions. These are referred to as the three-point, multi-disc and vasculature phantoms in the text.

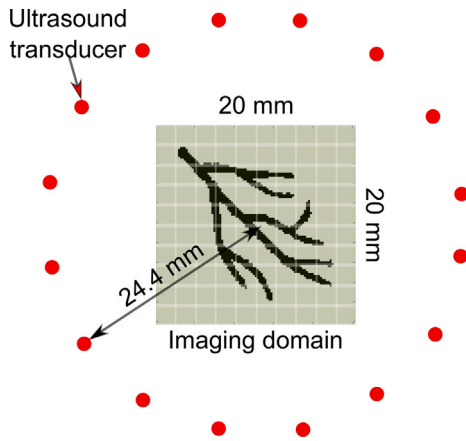


Fig. 2. Computational setup for forward data simulation in PAT.

The normalized pressure values are represented by the color bars, where black and white regions correspond to pressure values of 1 and 0 Pa, respectively. The first phantom consisted of three spherical sources of diameter 0.4 mm placed axially at distances 0, 3.2 and 6.4 mm, respectively from the center of the imaging domain of size $20 \times 20 \text{ mm}^2$. The spatial variation of tangential resolution of PAT imaging was studied using this phantom. The second phantom as given in Fig. 1(b) contained six spheres of different diameters (0.5, 0.6, 1.6, 2.0, 2.4 and 3.0 mm) and placed at different positions within the region of interest.

The vasculature phantom as shown in Fig. 1(c) was made by implementing a Monte Carlo method as described herein. At first, a binary image of a blood vessel network was scanned at a resolution of 600 dots per inch. The image size was $20 \times 20 \text{ mm}^2$ vis-a-vis 473×473 pixels. A value of 1 was marked for the pixels that contained the vasculature and 0 for the remaining pixels. The corresponding area covered by the vasculature was $\approx 39 \text{ mm}^2$. These pixels (with tag 1) were filled with RBCs approximated as spheres of radius $a = 2.92 \mu\text{m}$. A total of 579 037 such spheres were randomly placed within those pixels (with tag 1). The RSA method, which is a popular Monte Carlo algorithm, was used for this purpose (Saha, 2021; Berryman, 1983). Neither the cells inside the same pixel nor those of the neighboring pixels overlapped. The RBCs occupied an area of 15.5 mm^2 so that the hematocrit level was maintained at ≈ 0.4 . Therefore, it was indeed a sparse matrix/image but retained the microscopic details of the vascular structure. The same procedure was also realized in Prakash et al. (2020), Warbal and Saha (2022a), Saha (2021). This Monte Carlo approach for tissue simulation took nearly 2 min in a virtual machine [CentOS, Intel Core Processor (Broadwell, IBRS), 2.19 GHz, 256 GB RAM, and 80 cores]. Fig. 1(c) can be considered as a 2D cross-section of a 3D tissue.

3.1.2. Generation of forward data

A representative PAT simulation setup for generating the forward data is displayed in Fig. 2. For each phantom, opto-thermo-mechanical parameters such as I_0 , μ_a , β and C_p of the absorbers were taken as unity (Prakash et al., 2020). The speed of sound was fixed to $v_s = v_f = 1480 \text{ m/s}$; the density was considered as $\rho_s = \rho_f = 1000 \text{ kg/m}^3$. The scanning radius was taken as 24.4 mm. The position coordinates of all the individual sources were stored beforehand with respect to the coordinate system of the phantom. These coordinates relative to a detector were then determined by performing an appropriate coordinate transformation (Warbal and Saha, 2022a).

Assume a spherical PA source. A wide range of frequencies (0.001 to 1000 MHz with an increment of 0.01 MHz) were considered for calculating the PA signal for such a source by evaluating Eq. (7). The sampling frequency was set at 2000 MHz. The SIRF for that source

depending upon its position with respect to a detector (of diameter 10 mm) was estimated at the same sampling frequency. The functions, namely `xdc_piston` and `calc_h` of Field II were employed for this task (Jensen and Svendsen, 1992). The PA signal was convolved with the SIRF and stored in a long vector of size $1 \times 160\,000$ (this vector essentially corresponded to a time array of the same length having interval 0.5 ns and start time = 0 ns). In this way, the PA signals for all individual sources were calculated and appropriately (based on the start times) added with the long vector to generate the resultant PA signal. After that the resultant signal was filtered with the Gabor filter which mimicked a transducer with center frequency $f_0 = 2.25 \text{ MHz}$ and 70% as the fractional bandwidth. Further, the filtered PA signal was downsampled 80 times (Prakash et al., 2020). This process was repeated for 100 detectors uniformly placed over 0 to 2π . The size of the measurement matrix \mathcal{P} after the truncation was $60\,100 \times 1$. The computation time for PA signal simulation for 100 detectors for the first two phantoms was about 10 s whereas, it was approximately 29 h for the vasculature phantom in the same computer (virtual machine). The effect of sensor directivity was thus incorporated in this technique.

3.1.3. Formation of system matrix

The imaging domain [see Fig. 2] was divided into $101 \times 101 = 10\,201$ grid points with $dx = dy = 200 \mu\text{m}$. Therefore, the size of the \mathcal{X} matrix became $10\,201 \times 1$. The coordinates were stored relative to the coordinate system of the phantoms. At first, the PA signal from a sphere of radius $50 \mu\text{m}$ was computed. The SIRF for a particular detector and a grid point pair was also generated after the required coordinate transformation. The SIRF was convolved with that PA signal to obtain the signal emitted by that grid point and detected by the finite sensor. In the next step, filtering and downsampling were performed on this high-frequency signal. The downsampled signal was truncated between 100 and 700 time steps. Subsequently, the PA signals from all grid points captured by that detector were evaluated and filled into the \mathcal{A} matrix. The same procedure was realized for all the detectors. The size of the \mathcal{A} matrix would be $60\,100 \times 10\,201$. In this way, the \mathcal{A} matrix was constructed for the FDWD method. The time taken to build \mathcal{A} matrix for 100 detectors was about 7 h 20 min for a 10 mm transducer. The angular response of each detector for each grid point was incorporated within the system matrix in this approach. The system matrix for the PDs was also built. The PA signal emitted by that sphere was recorded as the reference signal. The scaling and shifting properties of the PA signal were utilized for computing the signals from all grid points and detectors. Those signals (after filtering and downsampling) were loaded into the system matrix. Building \mathcal{A} matrix for PDs took about 4 h 18 min. Note that the finite aperture size and directivity effects of the transducer were not incorporated in the PD scheme.

3.1.4. Reconstruction of PAT images

The initial pressure distribution was then computed using the three reconstruction algorithms. Eq. (17) was computed for reconstructing an image using the first technique. This was achieved by deploying the `csvd`, `l_curve` and Tikhonov functions available in the regularization toolbox (Hansen, 2007). The positivity constraint was enforced by replacing the negative gray scale values in the reconstructed image with zeros. In the second method, Eq. (18) was evaluated for obtaining the initial pressure map of the region of interest. The function `fista_lasso` of the FISTA toolbox was employed for this purpose and the positivity constraint was included by setting 'opts.pos' function as 'true' (Beck and Teboulle, 2009). The TVAL toolbox was utilized to implement Eq. (19) for image creation. Here, the 'opts.nonneg' must be set to 'true' for ensuring the non-negative gray values of a reconstructed image. An initial guess of λ for the first reconstruction protocol was determined by the L-curve method for each phantom. After that fine tuning of λ was carried out heuristically to obtain the best reconstructed image. In other words, the λ value was varied over a wide range — the initial guess was multiplied by a vector [0.00001, 0.0001, 0.001,

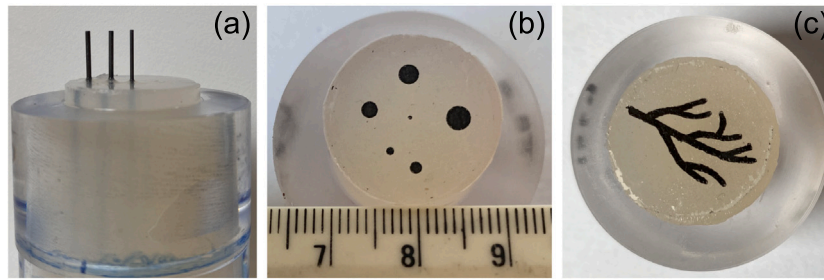


Fig. 3. Photographs of the phantoms used in the experimental study- (a) three-pencil-lead phantom, (b) multi-disc phantom and (c) vasculature phantom.

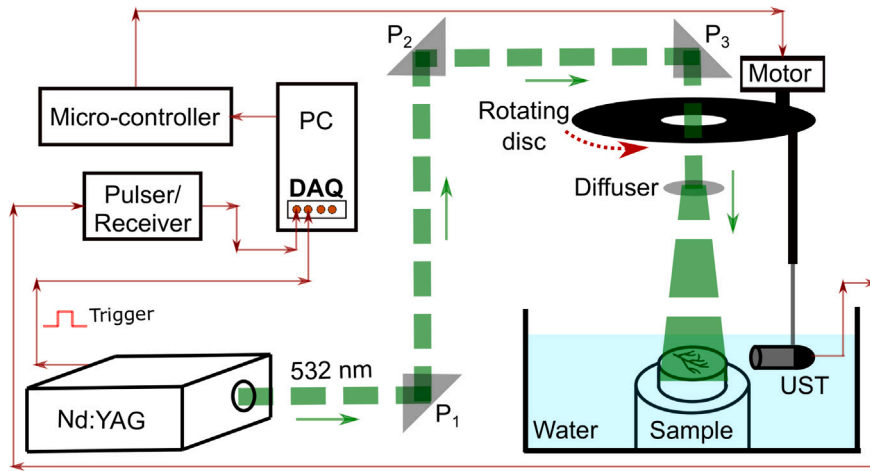


Fig. 4. Schematic diagram of the experimental setup.

0.01, 0.1, 1, 10, 100, 1000]. For each λ , an image was generated and the PCC value was computed with respect to the ground truth. The image with the highest PCC value was taken as the best image and the corresponding numerical value of the regularization parameter was considered the optimal value. Similarly, for the TV scheme, η and ζ values were tuned for finding out the best solution. The numerical values of η and ζ were altered as 2^n from $n = 4$ to 13. The images reconstructed using the FDWD method were compared with those of the PD approach. It might be mentioned here that the default configuration for convergence of each reconstruction algorithm was utilized in this work. The convergence criteria were found to be different for different algorithms. For example, the tolerance levels were $1e-12$, $1e-8$ and $1e-3$ for the l_2 , l_1 and TV regularization methods, respectively.

3.2. Experimental methods

3.2.1. Experimental phantoms

The PA signals from three experimental phantoms were collected. These phantoms were analogous to the numerical phantoms and the photographs are illustrated in Fig. 3. In the first phantom, three pencil leads were vertically placed at 0, 4, and 8 mm distances from the center of the phantom in a gelatin base (8% gelatin in distilled water). It was held in an acrylic cylinder (see Fig. 3(a)). To make the second and third phantoms, the multi-disc and vasculature structures were printed on transparent sheets and glued on the gelatin base as apparent from Figs. 3(b) and (c), respectively.

3.2.2. Experimental setup

A block diagram of the experimental setup for the PAT imaging is displayed in Fig. 4. A Q-switched Nd:YAG pulsed laser (NT352C-10-SH-H, Ekspla) emitting 532 nm wavelength was utilized to shine the samples. The duration of the light pulses was 6 ns and the repetition rate was 10 Hz. The energy per pulse was measured to be nearly 13.7

mJ/cm². Thus, the fluence was well under the ANSI safety limit (American National Standards Institute, 2022). The laser beam was guided through three right-angle uncoated prisms (P_1 , P_2 , and P_3 in Fig. 4) and one uncoated plano-concave lens (diffuser) to fall on the sample. The PA signals were measured by a single-element ultrasonic transducer with a center frequency of 2.25 MHz, a fractional bandwidth of 70% and a diameter of 10 mm (V325-SU, Panametric). The detected signals were amplified with 50 dB gain using a pulser/receiver (DPR300, JSR Ultrasonics). Thereafter, these signals were stored via a data acquisition card at a sampling frequency of 25 MHz (PCIe-9852, ADLINK). The scanning radius was approximately 24.4 mm. The speed of revolution of the ultrasonic transducer was set to 0.5 degree/s. The customized scanning system was manufactured by Holmarc, India.

3.2.3. Image formation

The pressure data at 100 detector locations were stacked in the \mathcal{P} matrix (long column vector). The PA signal for each detector position was obtained by averaging 20 radio frequency lines around that location. The same \mathcal{A} matrix built for the numerical study was employed for the image reconstruction with the l_2 norm, l_1 norm and TV minimization schemes. Two sets of images (for PD and FDWD) were formed and then compared. As we did in the previous case, the regularization parameter was first estimated through the L-curve method. After that it was varied over a large range. For each value, an image was formed and stored. To find out the best image, mean pixel value (MPV) was computed from a small region for each reconstructed image. The MPV is defined as,

$$MPV = \frac{p_1 + p_2 + p_3 + \dots + p_n}{n}, \quad (24)$$

where $p_1, p_2, p_3 \dots p_n$ are the pressure values belonging to that region. In this work, 36 pixels were involved for this calculation. These regions are marked by the red boxes in Figs. 8(a), 9(a), and 10(a). The image which provided the highest MPV was chosen as the best image and the corresponding numerical value of λ was taken as the optimal λ .

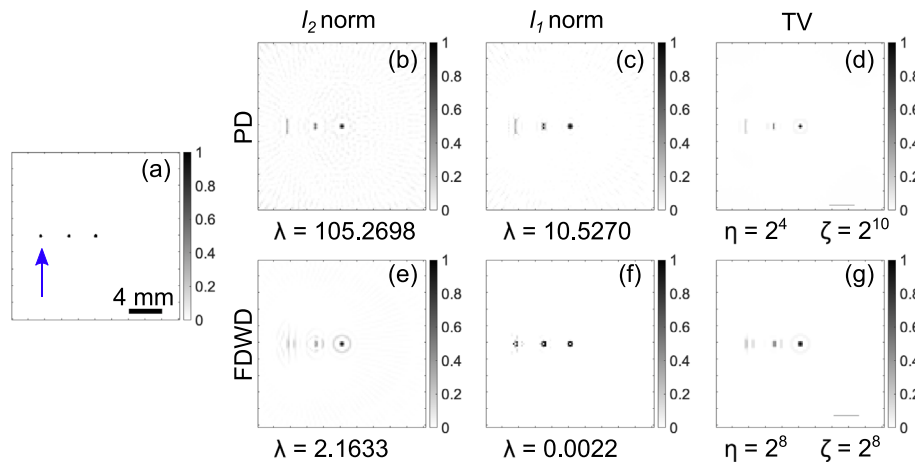


Fig. 5. (a) The ground truth of three-point phantom. (b)–(d) Normalized (by the maximum pressure value) reconstructed images utilizing the simulated forward data of a three-point phantom for the l_2 norm, l_1 norm and TV schemes, respectively, for a point detector (PD). The reconstructed images (e), (f) and (g) are same as that of (b), (c), and (d), respectively, but for a finite detector with directivity factor (FDWD). Images include color bars quantifying gray levels. The numerical values of λ , η and ζ are given at the bottom of the respective image.

4. Image reconstruction results

4.1. Computational results

Fig. 5 contains the reconstructed images of the three-point phantom. Each image is normalized with respect to its maximum pixel value. A color bar is provided alongside each image to show the numerical values of the gray levels. The images presented in the first row have been generated by assuming the transducers as the PDs. The images in the second row have been formed for the detector having a finite aperture (FDWD case). The outputs of the l_2 norm, l_1 norm and TV methods are inserted in the second, third and fourth columns of Fig. 5, respectively. The optimum value of the regularization parameter for a reconstruction approach is given at the bottom of the corresponding image. This value was chosen heuristically as explained earlier. Visually, the reconstructed images for the FDWD protocol are much better when compared to those of the PD technique. The numerical values of the quantitative metrics are given in Table 1 (rows 3 to 6). In the case of PD, significant blurring can be noticed in the peripheral region of the three-point phantom. Note that a point has become an arc. This is most prominently visible for the outermost point with respect to the scanning/imaging center. Therefore, the tangential resolution degrades as we move radially from the scanning/imaging center. In the case of FDWD, this degradation has been mitigated significantly. Though small blurring can be observed in Fig. 5(e), it is almost absent in Fig. 5(f) and (g). The numerical values of the metrics in Table 1 are not fully consistent with this observation. For example, numerical values become comparable for the first reconstruction method (see rows 3 to 6 and columns 3 and 4 in Table 1). Moreover, they demonstrate the opposite trend for the second and third methods (e.g., PCC and CNR values for the FDWD are smaller than those of the PD; see rows 4 and 5 and columns 5 to 8 of Table 1). The tangential resolution degradation can be quantified using the arc length metric (see row 3 of Table 2). The pixels with gray values above 0.1 in the normalized images were taken into account while calculating the arc length of a test shape [marked by an arrow in Fig. 5(a)]. The values are consistent with the visual interpretation of the images as the improvement can be seen in the tangential resolution (reduced arc length) for the FDWD scheme.

Similarly, the reconstructed images of the multi-disc phantom are displayed in Fig. 6. As described above, color bar is attached to each image. The quantitative estimation of the metrics are presented in Table 1 (rows 7 to 10). It can be seen from Figs. 6 (b)–(d) that the circular shapes are converted into elliptical shapes. Additionally, the black regions are surrounded by white rings. These distortions

Table 1

Image quality metrics estimated from the simulated images.

Phantom	Metrics	l_2 norm		l_1 norm		TV	
		PD	FDWD	PD	FDWD	PD	FDWD
Three-point	RMSE	0.029	0.027	0.028	0.038	0.024	0.027
	PCC	0.51	0.49	0.55	0.41	0.63	0.54
	CNR	39.13	36.76	43.52	29.52	52.35	42.18
	SSIM	0.95	0.98	0.98	0.98	0.99	0.99
Multi-disc	RMSE	0.133	0.162	0.110	0.163	0.145	0.141
	PCC	0.80	0.60	0.88	0.66	0.75	0.74
	CNR	13.12	7.45	18.81	8.85	11.31	11.05
	SSIM	0.79	0.52	0.89	0.82	0.83	0.76
Vasculature	RMSE	0.276	0.217	0.252	0.221	0.252	0.166
	PCC	0.57	0.82	0.66	0.85	0.67	0.92
	CNR	4.29	9.03	5.46	10.11	5.63	14.78
	SSIM	0.39	0.67	0.48	0.75	0.54	0.89

are almost completely removed when the FDWD method works in conjunction with the first two model based algorithms [see Figs. 6(e) and (f)]. The TV scheme partially eliminates these distortions [see Fig. 6(g)]. Therefore, it is clear that the FDWD technique in general provides a better map of the initial pressure distribution for this phantom compared to the PD approach. However, the estimated numerical values of the image quality metrics in Table 1 demonstrate that the PD procedure works better than the FDWD process and thus contradicts the visual finding. It seems that these global parameters are not properly reflecting the local improvements. In order to accurately quantify visual distortions, the aspect ratio parameter was calculated for a PA source [denoted by an arrow in Fig. 6(a)]. For this analysis, only pixels exhibiting normalized pressure values exceeding 0.1 were taken into account along both the lateral (major axis) and axial (minor axis) directions. The aspect ratio was computed as the ratio of the major axis to the minor axis. It is clear from row 4 of Table 2 that the aspect ratio for each PD image retains higher value whereas that of FDWD method is close to 1, proving that shapes are better reconstructed in the FDWD scheme compared to the PD procedure.

The reconstructed images of the vasculature phantom are pasted in Fig. 7. The numerical values of gray shades can be estimated from the associated color bar. Table 1 (rows 11 to 14) elaborates the numerical values of the image quality parameters for this phantom. The vascular structure is reproduced well in the central part of the imaging region for all reconstruction algorithms for the PD protocol [see Figs. 7(b)–(d)]. Nevertheless, the shape is not restored properly in the peripheral region. Figs. 7(e)–(g) show that accurate reproduction of the structure is

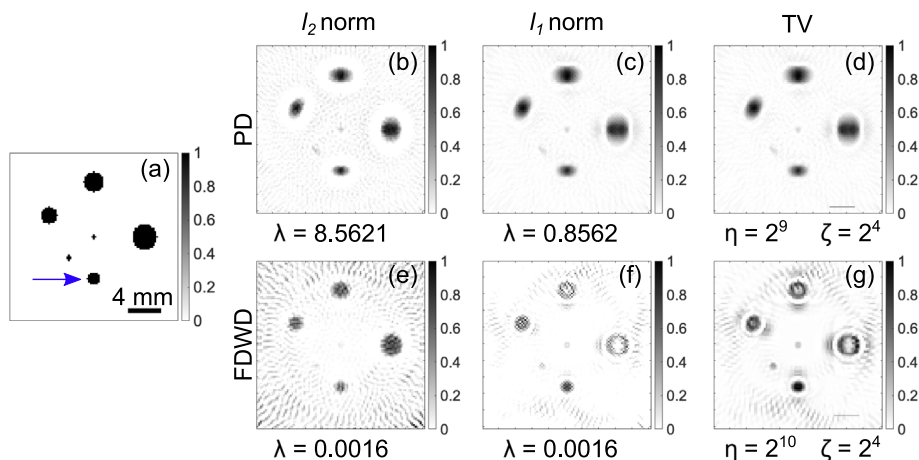


Fig. 6. Ground truth and normalized reconstructed images same as that of Fig. 5 but for a multi-disc phantom.

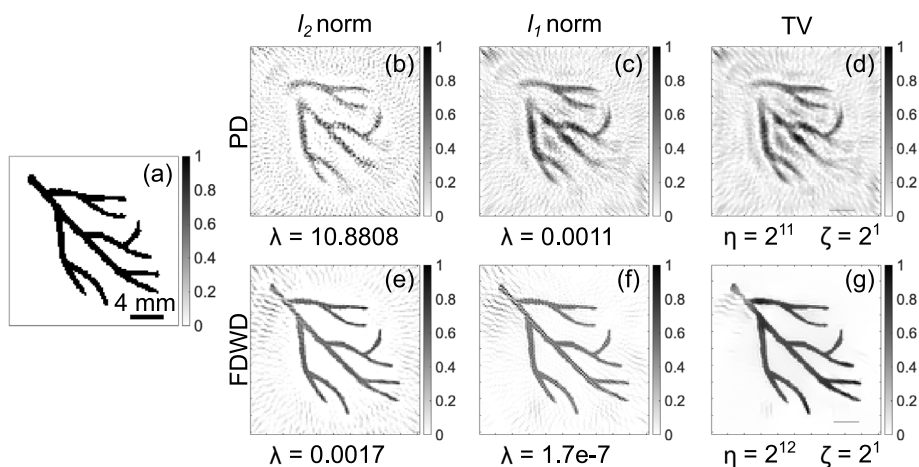


Fig. 7. Demonstration of the ground truth and reconstructed images (normalized) same as Fig. 5 but for a vasculature phantom.

Table 2
Computed values of arc length and aspect ratio for the three-point and multi-disc phantoms.

	Phantom	Metrics	l_2 norm		l_1 norm		TV	
			PD	FDWD	PD	FDWD	PD	FDWD
Simulation	Three-point	Arc length (mm)	1.8	1.0	1.8	1.0	1.8	1.0
	Multi-disc	Aspect ratio	1.83	1.12	1.62	1.0	1.86	1.12
Experiment	Three-point	Arc length (mm)	2.8	1.2	2.4	1.4	2.4	1.4
	Multi-disc	Aspect ratio	1.22	1.00	1.08	1.00	1.36	0.91

possible when the effect of directivity is incorporated within the system matrix (i.e., FDWD method). The RMSE is less for the latter method compared to the former scheme as evident from Table 1 (compare columns 3 and 4 of row 11). The variation of other parameters is also in accordance with this observation (PCC, CNR and SSIM values increase as the reconstruction approach is changed from PD to FDWD; columns 3 and 4 of rows 12, 13, 14). Among, the three reconstruction strategies, l_1 norm and TV methods are better than the l_2 norm technique.

4.2. Experimental results

The reconstructed images of the experimental phantoms shown in Fig. 3 or 8(a) have been generated by the PD and FDWD schemes employing the reconstruction methods stated above. The normalized reconstructed images for the pencil-lead phantom are provided in Figs. 8(b)–(g). A color bar is included next to each image to visually depict the numerical values of different gray levels. Figs. 8(b)–(d) correspond

to the PD method and Figs. 8(e)–(g) belong to the FDWD protocol. The respective images for l_2 norm, l_1 norm and TV methods are arranged in the second, third and fourth columns, respectively. The numerical values of λ , η and ζ parameters are included at the bottom of the respective images. The region marked by the red box has been used for calculating the MPV [see Fig. 8(b)]. Figs. 8(b)–(d) show that the shape of the tips of the first two pencil leads (from the center) are reproduced well. However, the tip of the farthest pencil lead elongates in the tangential direction which is a signature of degradation of the tangential resolution. The shapes of the tips are much better restored in Figs. 8(e)–(g). This is estimated by quantifying the arc length as described previously. The 4th row of Table 2 demonstrates that the arc length is substantially reduced in the FDWD method compared to its counterpart. The noise level in the peripheral regions of Figs. 8(e)–(g) is slightly higher than that of Figs. 8(b)–(d). Therefore, improved PAT imaging is possible by the FDWD method (without deterioration of the tangential resolution).

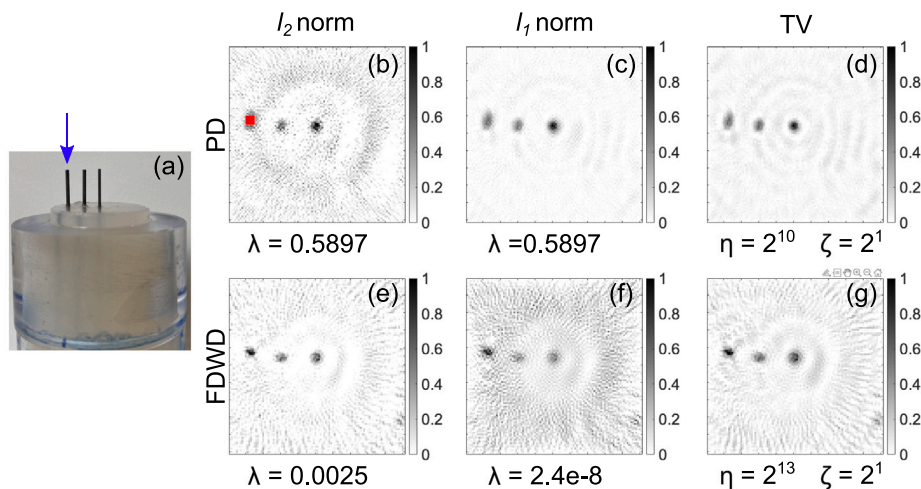


Fig. 8. (a) Photograph of a three-pencil-lead phantom. (b)–(d) Reconstructed images based on the measured PA signals of a three-pencil-lead phantom (normalized by the maximum pressure value) for the l_2 norm, l_1 norm and TV techniques, respectively, in the case of the PD scheme. The reconstructed images (e)–(g) are same as (b)–(d) but for the FDWD case. The quantitative values of gray shades can be found from the color bar for each image. The numerical values of λ , η and ζ are pasted below the respective images. The red box in (b) is the region of interest to compute MPV for this phantom.

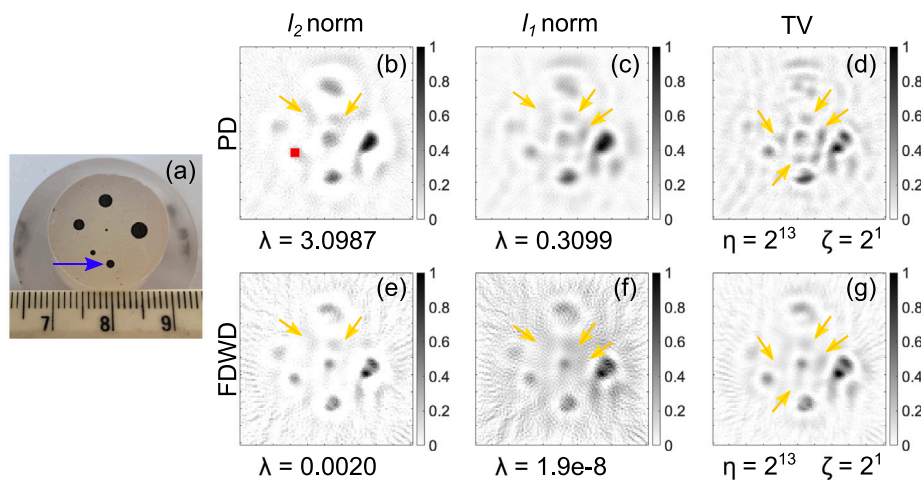


Fig. 9. (a) Photograph of a printed multi-disc phantom. Normalized reconstructed images are arranged in the same manner as of Fig. 8 but for a printed multi-disc phantom. Comparison of regions pointed by the arrows in a pair of images [(b) and (e); (c) and (f); (d) and (g)].

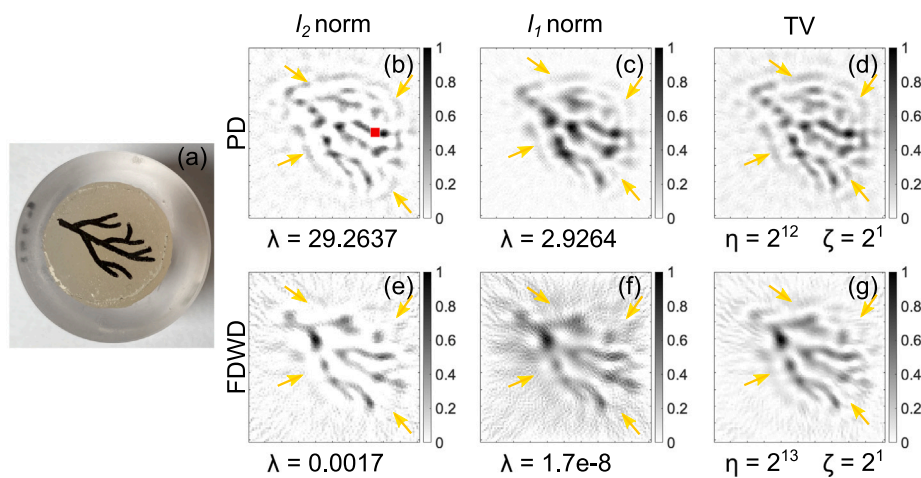


Fig. 10. (a) Photograph of a printed vasculature phantom. Display of the reconstructed images (normalized) similar to Fig. 8 but for a printed vasculature phantom. Comparison of sectors marked by the arrows in a pair of images [(b) and (e); (c) and (f); (d) and (g)].

The best images of the multi-disc phantom are portrayed in Fig. 9 (including color bars). Here also, the shapes of the PA sources are better reproduced in the FDWD scheme than the PD approach. The aspect ratio of a test object [indicated by an arrow in Fig. 9(a)] is computed to be close to 1 for the FDWD algorithm, however, that of the PD procedure deviates much from 1 (see 5th row of Table 2). Some unwanted shades prominently arise in the PD images but they appear faintly in the FDWD images [compare the regions pointed by the arrows in Figs. 9(b) and (e); Figs. 9(c) and (f); Figs. 9(d) and (g)]. The same observation can also be made for the vasculature phantom as displayed in Fig. 10. Color bars are incorporated for quantitative estimation of gray levels. The FDWD method significantly removes image blurring and artifacts. The corresponding regions in the images are marked by the arrows [compare Figs. 10(b) and (e); Figs. 10(c) and (f); Figs. 10(d) and (g)]. However, the contrast level of the vascular branches in the FDWD images is on the lower side with respect to the PD images.

5. Discussion and conclusions

In this work, both computational and experimental studies are carried out to evaluate the effect of sensor directivity on PAT imaging. As mentioned above, a similar problem was also dealt with previously and reported in Wang et al. (2010). To generate the blood vessel network phantom, we used a popular Monte Carlo algorithm called the random sequential adsorption technique. This is a very simple algorithm and works well when the packing fraction is low (up to 0.5). It may not converge at higher concentrations of particles. The reason behind this is that valid (or accepted) locations of solid spheres become fixed and minor adjustments of positions are not possible resisting compact packing of spheres. This issue can be resolved by applying the Metropolis algorithm. In this algorithm, the positions of all the spheres are refreshed sequentially to attain the minimum energy state of the system. Consequently, dense packing is possible. Construction of a tissue realization appears to be very fast (≈ 2 min) exploiting the Monte Carlo method.

The PA signals emitted by the individual spherical absorbers can be easily evaluated by utilizing the exact or approximate method (Saha, 2021; Berryman, 1983). The physical properties (e.g., acoustic inhomogeneity, size and shape dispersity) of each absorber can be taken into account at this stage. The frequency dependent acoustic attenuation of the extracellular matrix can also be included in this approach. The discrete particle approach allows to elegantly couple the PA signal emitted by an absorber with the SIRF of the detector (by which the measurement is performed). Accordingly, the resultant PA signal from the tissue has been obtained by linearly summing the contributions from the individual sources. Therefore, forward data simulation retaining the impact of a realistic transducer becomes straightforward and very fast. Herein, the transducer has been assumed as a plane piston and mounted on a rigid baffle. The Field II toolbox has been utilized to calculate the SIRF of such an ultrasonic sensor. It is a robust toolbox and enables us to calculate SIRF for various types of transducers — plane piston mounted on a rigid/soft baffle, focused transducer, apodized transducer, array transducer, etc.

A single element, unfocused transducer changes the width and magnitude of the acoustic pulse depending upon its origin in space. Therefore, these features remain embedded within the forward data if a transducer with a finite aperture is used for signal collection. The pulse broadening results in image blurring in the PAT modality if it is not compensated appropriately. In this work, we build the system matrix by including the response of a realistic transducer (FDWD approach). It is intuitively expected that the effect of sensor directivity would be canceled out during the matrix inversion step providing PAT imaging devoid of sensor directivity effect. A point detector is assumed to respond omni-directionally to the incoming acoustic signals. It also does not alter the width of each signal (widths of the input and output pulses are the same). Therefore, the corresponding system matrix does

not include pulse elongation. Hence, the PD approach cannot compensate for pulse stretching present in the forward data during image reconstruction and therefore, produces blurry images.

This study employs l_2 norm-, l_1 norm- and TV- based regularization methods for PAT image generation (Prakash et al., 2018). As pointed out earlier, a closed form analytical solution of Eq. (12) can be derived under the framework of l_2 norm based Tikhonov regularization. Nevertheless, this is not possible for the remaining methods and hence, numerical solutions may be obtained. Many different third party softwares are available freely and those can be deployed for obtaining solutions exploring these frameworks. The regularization toolbox is used in the present work for the first algorithm whereas FISTA and TVAL toolboxes are utilized for the second and third protocols, respectively. Note that another toolbox known as the SALSA has also been utilized for PAT imaging (Prakash et al., 2018). All these toolboxes essentially involve variants of the Lagrange multiplier method for solving constrained optimization problems. Each of these methods desires to reduce computational complexity and attain accurate solutions as fast as possible. It may be mentioned here that for the PD scheme, the execution times in the l_2 norm, l_1 norm and TV procedures were found to be 251 (including the time required for SVD = 239 s), 54 and 182 seconds, respectively for the same virtual machine. On the other hand, the same techniques took 268 (SVD time = 257 s), 80 and 159 seconds, respectively for the FDWD approach. These numerical values depict that the second and third methods execute faster than the first algorithm. Moreover, the first method is known to penalize edges and thus may induce over-smoothing effect (sharp boundaries may be lost). The second and third algorithms do not penalize the edges and thus boundaries may be restored well in the reconstructed image. Further, it is seen that the reconstructed images contain streak artifacts, which arise due to sparse spatial sampling. Dense spatial sampling can remove such artifacts (Hu et al., 2020, 2022). However, in that case, the size of the \mathcal{A} will become large posing huge computational burden.

In a typical time-domain PA model-matrix, the number of effective time samples generated by the light-absorbing structures is generally small. As a result, the \mathcal{A} matrix exhibits sparsity, with a very small number of non-zero entries. Including this aspect, the PA inverse problem has been successfully addressed using a matrix-free approach. Ding et al. presented a novel 3D model-based reconstruction method suitable for PAT imaging systems that utilize detection elements of arbitrary size and shape. To address the computational complexity and memory constraints, they developed an efficient implementation of the iterative inversion process using a graphic processing unit (GPU). They performed on-the-fly calculations of the model-matrix entries through a compact look-up table. The need for storing matrices can thus be avoided making the approach feasible and resource-efficient (Ding et al., 2020, 2017). We consider the possibility of implementing such an approach in our future endeavors.

In conclusion, a theoretical model for calculation of the PA signal from a tissue is presented. It essentially exploits the cellular aspect of tissue. The PA signals from cells approximated as spheres are computed using the exact method. Such a signal is convolved with the SIRF of a finite detector. The convolved signals are linearly summed up to obtain the resultant signal generated by a tissue. This is called the discrete particle approach which has been used here to simulate the PA signals from various numerical phantoms including a blood vessel network. This theoretical framework is essentially derived by drawing analogy with the model used to study ultrasonic scattering from tissue. A Monte Carlo algorithm has been implemented to construct the vasculature phantom by randomly placing spheres mimicking cells within the vasculature region. This approach allows to know spatial organization of cells (i.e., microscopic details) of the vasculature phantom. The simulated signals are used to form PAT images of the phantoms utilizing three model matrix inversion methods, namely, l_2 norm based regularization, l_1 norm based regularization and TV minimization procedures. The model matrix has been built by incorporating the directivity effect of

a finite detector. Another model matrix has been formed by assuming finite detector as a point sensor and accordingly, images have been generated for comparison. Analogous phantom-experiments have been conducted as well. Both the numerical and experimental results suggest that much improved PAT imaging is possible when the first type of model matrix (including directivity effect of finite detector) works in conjunction with the TV minimization scheme. This combination can be utilized in practice for faithful image reconstruction of vasculature structures using PAT.

Declaration of competing interest

The authors declare that they have no known competing financial interests or personal relationships that could have appeared to influence the work reported in this paper.

Data availability

Data will be made available on request.

Acknowledgments

All the computational work reported in this paper was performed on the Central Computing Facility of IIIT Allahabad. This work was supported in part by the ICMR, India (# 56/2/2020-Hae/BMS) and DBT, India (# BT/PR44547/MED/32/791/ 2021) grants. We would like to thank Dr Manish Bhatt for stimulating discussions. The authors would also like to thank Subhadip, Ujjal, Sudeep and Zartab for their support during the work.

References

- Afonso, M.V., Bioucas-Dias, J.M., Figueiredo, M.A., 2010. An augmented Lagrangian approach to the constrained optimization formulation of imaging inverse problems. *IEEE Trans. Image Process.* 20 (3), 681–695.
- American National Standards Institute, 2022. American National Standard for Safe Use of Lasers. Laser Institute of America.
- Araque Caballero, M.A., 2013. Incorporating Sensor Properties in Optoacoustic Imaging (Doctoral dissertation). Technische Universität München.
- Beck, A., Teboulle, M., 2009. A fast iterative shrinkage-thresholding algorithm for linear inverse problems. *SIAM J. Imaging Sci.* 2 (1), 183–202.
- Berryman, J.G., 1983. Random close packing of hard spheres and disks. *Phys. Rev. A* 27 (2), 1053.
- Bohndiek, S.E., Sasportas, L.S., Machtaler, S., Jokerst, J.V., Hori, S., Gambhir, S.S., 2015. Photoacoustic tomography detects early vessel regression and normalization during ovarian tumor response to the antiangiogenic therapy trebananib. *J. Nucl. Med.* 56 (12), 1942–1947.
- Chowdhury, K.B., Prakash, J., Karlas, A., Jüstel, D., Ntziachristos, V., 2020. A synthetic total impulse response characterization method for correction of hand-held optoacoustic images. *IEEE Trans. Med. Imaging* 39 (10), 3218–3230.
- Cox, B.T., Treeby, B.E., 2010. Effect of sensor directionality on photoacoustic imaging: a study using the k-wave toolbox. In: *Photons Plus Ultrasound: Imaging and Sensing 2010*, Vol. 7564. SPIE, pp. 123–128.
- Daubechies, I., Defrise, M., De Mol, C., 2004. An iterative thresholding algorithm for linear inverse problems with a sparsity constraint. *Comm. Pure Appl. Math. J. Issued Courant Inst. Math. Sci.* 57 (11), 1413–1457.
- Ding, L., Dean-Ben, X.L., Razansky, D., 2017. Efficient 3-D model-based reconstruction scheme for arbitrary optoacoustic acquisition geometries. *IEEE Trans. Med. Imaging* 36 (9), 1858–1867.
- Ding, L., Razansky, D., Dean-Ben, X.L., 2020. Model-based reconstruction of large three-dimensional optoacoustic datasets. *IEEE Trans. Med. Imaging* 39 (9), 2931–2940.
- Goldstein, T., Studer, C., Baraniuk, R., 2014. A field guide to forward-backward splitting with a FASTA implementation. *arXiv preprint arXiv:1411.3406*.
- González, G., Kolehmainen, V., Seppänen, A., 2017. Isotropic and anisotropic total variation regularization in electrical impedance tomography. *Comput. Math. Appl.* 74 (3), 564–576.
- Guo, Z., Li, C., Song, L., Wang, L.V., 2010. Compressed sensing in photoacoustic tomography in vivo. *J. Biomed. Opt.* 15 (2), 021311–021311.
- Han, Y., Tzoumas, S., Nunes, A., Ntziachristos, V., Rosenthal, A., 2015. Sparsity-based acoustic inversion in cross-sectional multiscale optoacoustic imaging. *Med. Phys.* 42 (9), 5444–5452.
- Hansen, P.C., 2007. Regularization tools version 4.0 for Matlab 7.3. *Numer. Algorithms* 46, 189–194.
- Hansen, P.C., O’Leary, D.P., 1993. The use of the L-curve in the regularization of discrete ill-posed problems. *SIAM J. Sci. Comput.* 14 (6), 1487–1503.
- Hu, P., Li, L., Lin, L., Wang, L.V., 2020. Spatiotemporal antialiasing in photoacoustic computed tomography. *IEEE Trans. Med. Imaging* 39 (11), 3535–3547.
- Hu, P., Li, L., Wang, L.V., 2022. Location-dependent spatiotemporal antialiasing in photoacoustic computed tomography. *IEEE Trans. Med. Imaging* 42 (4), 1210–1224.
- Jensen, J.A., Svendsen, N.B., 1992. Calculation of pressure fields from arbitrarily shaped, apodized, and excited ultrasound transducers. *IEEE Trans. Ultrason. Ferroelectr. Freq. Control* 39 (2), 262–267.
- Karmakar, S., Hysi, E., Kolios, M.C., Saha, R.K., 2015. Realistic photoacoustic image simulations of collections of solid spheres using linear array transducer. In: *Photons Plus Ultrasound: Imaging and Sensing 2015*, Vol. 9323. SPIE, pp. 493–500.
- Kong, Q., Gong, R., Liu, J., Shao, X., 2018. Investigation on reconstruction for frequency domain photoacoustic imaging via TVAL3 regularization algorithm. *IEEE Photonics J.* 10 (5), 1–15.
- Li, D., Humayun, L., Vienneau, E., Vu, T., Yao, J., 2021. Seeing through the skin: Photoacoustic tomography of skin vasculature and beyond. *JID Innovations* 1 (3), 100039.
- Li, M.L., Tseng, Y.C., Cheng, C.C., 2010. Model-based correction of finite aperture effect in photoacoustic tomography. *Opt. Express* 18 (25), 26285–26292.
- Li, C., Yin, W., Jiang, H., Zhang, Y., 2013. An efficient augmented Lagrangian method with applications to total variation minimization. *Comput. Optim. Appl.* 56, 507–530.
- Li, L., Zhu, L., Ma, C., Lin, L., Yao, J., Wang, L., Maslov, K., Zhang, R., Chen, W., Shi, J., Wang, L.V., 2017. Single-impulse panoramic photoacoustic computed tomography of small-animal whole-body dynamics at high spatiotemporal resolution. *Nat. Biomed. Eng.* 1 (5), 0071.
- Lin, L., Hu, P., Shi, J., Appleton, C.M., Maslov, K., Li, L., Zhang, R., Wang, L.V., 2018. Single-breath-hold photoacoustic computed tomography of the breast. *Nature Commun.* 9 (1), 2352.
- Lu, T., Wang, Y., Li, J., Prakash, J., Gao, F., Ntziachristos, V., 2020. Full-frequency correction of spatial impulse response in back-projection scheme using space-variant filtering for optoacoustic mesoscopy. *Photoacoustics* 19, 100193.
- Lv, X.G., Song, Y.Z., Wang, S.X., Le, J., 2013. Image restoration with a high-order total variation minimization method. *Appl. Math. Model.* 37 (16–17), 8210–8224.
- Manohar, S., Dantuma, M., 2019. Current and future trends in photoacoustic breast imaging. *Photoacoustics* 16, 100134.
- Na, S., Zhang, Y., Wang, L.V., 2022. Cross-ray ultrasound tomography and photoacoustic tomography of cerebral hemodynamics in rodents. *Adv. Sci.* 9 (25), 2201104.
- Nandy, S., Mostafa, A., Hagemann, I.S., Powell, M.A., Amidi, E., Robinson, K., Mutch, G.M., Siegel, C., Zhu, Q., 2018. Evaluation of ovarian cancer: initial application of coregistered photoacoustic tomography and US. *Radiology* 289 (3), 740–747.
- Nyayapathi, N., Lim, R., Zhang, H., Zheng, W., Wang, Y., Tiao, M., Oh, K.W., Fan, X.C., Bonaccio, E., Takabe, K., Xia, J., 2019. Dual scan mammoscope (DSM)—a new portable photoacoustic breast imaging system with scanning in cranio-caudal plane. *IEEE Trans. Biomed. Eng.* 67 (5), 1321–1327.
- Paltauf, G., Viator, J.A., Prah, S.A., Jacques, S.L., 2002. Iterative reconstruction algorithm for optoacoustic imaging. *J. Acoust. Soc. Am.* 112 (4), 1536–1544.
- Prakash, R., Badal, D., Paul, A., Sonker, D., Saha, R.K., 2020. Photoacoustic signal simulation using discrete particle approach and its application in tomography. *IEEE Trans. Ultrason. Ferroelectr. Freq. Control* 68 (3), 707–717.
- Prakash, J., Raju, A.S., Shaw, C.B., Pramanik, M., Yalavarthy, P.K., 2014. Basis pursuit deconvolution for improving model-based reconstructed images in photoacoustic tomography. *Biomed. Opt. Express* 5 (5), 1363–1377.
- Prakash, J., Sanny, D., Kalva, S.K., Pramanik, M., Yalavarthy, P.K., 2018. Fractional regularization to improve photoacoustic tomographic image reconstruction. *IEEE Trans. Med. Imaging* 38 (8), 1935–1947.
- Pramanik, M., 2014. Improving tangential resolution with a modified delay-and-sum reconstruction algorithm in photoacoustic and thermoacoustic tomography. *J. Opt. Soc. Am. A* 31 (3), 621–627.
- Pramanik, M., Ku, G., Wang, L.V., 2009. Tangential resolution improvement in thermoacoustic and photoacoustic tomography using a negative acoustic lens. *J. Biomed. Opt.* 14 (2), 024028–024028.
- Ramani, S., Liu, Z., Rosen, J., Nielsen, J.F., Fessler, J.A., 2012. Regularization parameter selection for nonlinear iterative image restoration and MRI reconstruction using GCV and SURE-based methods. *IEEE Trans. Image Process.* 21 (8), 3659–3672.
- Roitner, H., Haltmeier, M., Nuster, R., O’Leary, D.P., Berer, T., Paltauf, G., Grün, H., Burgholzer, P., 2014. Deblurring algorithms accounting for the finite detector size in photoacoustic tomography. *J. Biomed. Opt.* 19 (5), 056011–056011.
- Rosenthal, A., Razansky, D., Ntziachristos, V., 2010. Fast semi-analytical model-based acoustic inversion for quantitative optoacoustic tomography. *IEEE Trans. Med. Imaging* 29 (6), 1275–1285.
- Saha, R.K., 2021. Solving time-independent inhomogeneous optoacoustic wave equation numerically with a modified green’s function approach. *J. Acoust. Soc. Am.* 149 (6), 4039–4048.
- Sangha, G.S., Hu, B., Li, G., Fox, S.E., Sholl, A.B., Brown, J.Q., Goergen, C.J., 2022. Assessment of photoacoustic tomography contrast for breast tissue imaging using 3D correlative virtual histology. *Sci. Rep.* 12 (1), 2532.

- Schoonover, R.W., Wang, L.V., Anastasio, M.A., 2012. Numerical investigation of the effects of shear waves in transcranial photoacoustic tomography with a planar geometry. *J. Biomed. Opt.* 17 (6), 061215-061215.
- Seeger, M., Soliman, D., Aguirre, J., Diot, G., Wierzbowski, J., Ntziachristos, V., 2020. Pushing the boundaries of optoacoustic microscopy by total impulse response characterization. *Nat. Commun.* 11 (1), 2910.
- Shung, K.K., Thieme, G.A., 1992. *Ultrasonic Scattering in Biological Tissues*. CRC Press.
- Song, X., Pogue, B.W., Jiang, S., Dooley, M.M., Dehghani, H., Tosteson, T.D., Paulsen, K.D., 2004. Automated region detection based on the contrast-to-noise ratio in near-infrared tomography. *Appl. Opt.* 43 (5), 1053-1062.
- Szabo, T.L., 2004. *Diagnostic Ultrasound Imaging: Inside Out*. Academic Press.
- Thung, K.H., Raveendran, P., 2009. A survey of image quality measures. In: 2009 International Conference for Technical Postgraduates. TECHPOS, IEEE, pp. 1-4.
- Treeby, B.E., Cox, B.T., 2009. Fast tissue-realistic models of photoacoustic wave propagation for homogeneous attenuating media. In: *Photons Plus Ultrasound: Imaging and Sensing 2009*, Vol. 7177. SPIE, pp. 311-320.
- Treeby, B.E., Cox, B.T., 2010. k-Wave: MATLAB toolbox for the simulation and reconstruction of photoacoustic wave fields. *J. Biomed. Opt.* 15 (2), 021314-021314.
- Wagner, R.F., Insana, M.F., Brown, D.G., Hall, T., 1987. Describing small-scale structure in random media using pulse-echo ultrasound. *J. Opt. Soc. Am. A* 4, 910-922.
- Wang, L.V. (Ed.), 2017. *Photoacoustic Imaging and Spectroscopy*. CRC press.
- Wang, Z., Bovik, A.C., Sheikh, H.R., Simoncelli, E.P., 2004a. Image quality assessment: from error visibility to structural similarity. *IEEE Trans. Image Process.* 13 (4), 600-612.
- Wang, K., Ermilov, S.A., Su, R., Brecht, H.P., Oraevsky, A.A., Anastasio, M.A., 2010. An imaging model incorporating ultrasonic transducer properties for three-dimensional optoacoustic tomography. *IEEE Trans. Med. Imaging* 30 (2), 203-214.
- Wang, Y., Xing, D., Zeng, Y., Chen, Q., 2004b. Photoacoustic imaging with deconvolution algorithm. *Phys. Med. Biol.* 49 (14), 3117.
- Warbal, P., Pramanik, M., Saha, R.K., 2019. Impact of sensor apodization on the tangential resolution in photoacoustic tomography. *J. Opt. Soc. Am. A* 36 (2), 245-252.
- Warbal, P., Saha, R.K., 2022a. In silico evaluation of the effect of sensor directivity on photoacoustic tomography imaging. *Optik* 252, 168305.
- Warbal, P., Saha, R.K., 2022b. Performance comparison of commonly used photoacoustic tomography reconstruction algorithms under various blurring conditions. *J. Modern Opt.* 69 (9), 487-501.
- Wood, S.N., 2004. Stable and efficient multiple smoothing parameter estimation for generalized additive models. *J. Amer. Statist. Assoc.* 99 (467), 673-686.
- Xia, J., Wang, L.V., 2012. Photoacoustic tomography of the brain. In: *Optical Methods and Instrumentation in Brain Imaging and Therapy*. Springer New York, New York, NY, pp. 137-156.
- Xu, M., Wang, L.V., 2005. Universal back-projection algorithm for photoacoustic computed tomography. *Phys. Rev. E* 71 (1), 016706.
- Yang, X., Li, M.L., Wang, L.V., 2007. Ring-based ultrasonic virtual point detector with applications to photoacoustic tomography. *Appl. Phys. Lett.* 90 (25).
- Yao, L., Jiang, H., 2011. Enhancing finite element-based photoacoustic tomography using total variation minimization. *Appl. Opt.* 50 (25), 5031-5041.
- Yao, J., Wang, L.V., 2018. Recent progress in photoacoustic molecular imaging. *Curr. Opin. Chem. Biol.* 45, 104-112.
- Yao, J., Wang, L.V., 2021. Perspective on fast-evolving photoacoustic tomography. *J. Biomed. Opt.* 26 (6), 060602-060602.